remote sensing

MDPI

Article

Monitoring Salinity in Inner Mongolian Lakes Based on Sentinel-2 Images and Machine Learning

Mingming Deng [1,2], Ronghua Ma [1,3,*], Steven Arthur Loiselle [4], Minqi Hu [1], Kun Xue [1], Zhigang Cao [1], Lixin Wang [5], Chen Lin [1] and Guang Gao [1]

[1] Key Laboratory of Lake and Watershed Science for Water Security, Nanjing Institute of Geography and Limnology, Chinese Academy of Sciences, Nanjing 210008, China; mmdeng@niglas.ac.cn (M.D.); mqhu@niglas.ac.cn (M.H.); kxue@niglas.ac.cn (K.X.); zgcao@niglas.ac.cn (Z.C.); clin@niglas.ac.cn (C.L.); guanggao@niglas.ac.cn (G.G.)
[2] University of Chinese Academy of Sciences, Beijing 100049, China
[3] University of Chinese Academy of Sciences, Nanjing 211135, China
[4] Dipartimento di Biotecnologie, Chimica e Farmacia, CSGI, University of Siena, 53100 Siena, Italy; steven.loiselle@unisi.it
[5] School of Ecology and Environment, Inner Mongolia University, Hohhot 010021, China; lxwang@imu.edu.cn
* Correspondence: rhma@niglas.ac.cn; Tel.: +86-138-5155-4692

Abstract: Salinity is an essential parameter for evaluating water quality and plays a crucial role in maintaining the stability of lake ecosystems, particularly in arid and semi-arid climates. Salinity responds to changes in climate and human activity, with significant impacts on water quality and ecosystem services. In this study, Sentinel-2A/B Multi-Spectral Instrument (MSI) images and quasi-synchronous field data were utilized to estimate lake salinity using machine learning approaches (i.e., XGB, CNN, DNN, and RFR). Atmospheric correction for MSI images was tested using six processors (ACOLITE, C2RCC, POLYMER, MUMM, iCOR, and Sen2Cor). The most accurate model and atmospheric correction method were found to be the extreme gradient boosting tree combined with the ACOLITE correction algorithm. These were used to develop a salinity model (N = 70, mean absolute percentage error = 9.95%) and applied to eight lakes in Inner Mongolia from 2016 to 2024. Seasonal and interannual variations were explored, along with an examination of potential drivers of salinity changes over time. Average salinities in the autumn and spring were higher than in the summer. The highest salinities were observed in the lake centers and tended to be consistent and homogeneous. Interannual trends in salinity were evident in several lakes, influenced by evaporation and precipitation. Climate factors were the primary drivers of interannual salinity trends in most lakes.

Keywords: lake salinity; Sentinel-2A/B; machine learning; pattern; driving factors

Citation: Deng, M.; Ma, R.; Loiselle, S.A.; Hu, M.; Xue, K.; Cao, Z.; Wang, L.; Lin, C.; Gao, G. Monitoring Salinity in Inner Mongolian Lakes Based on Sentinel-2 Images and Machine Learning. *Remote Sens.* **2024**, *16*, 3881. https://doi.org/10.3390/rs16203881

Academic Editor: Dino Ienco

Received: 28 September 2024
Revised: 14 October 2024
Accepted: 14 October 2024
Published: 18 October 2024

1. Introduction

Salinity is an essential parameter for evaluating water quality and plays a crucial role in maintaining the stability of lake ecosystems, in particular, in arid and semi-arid climates. Changes in salinity impact species richness, functional diversity, habitat quality, water resource utilization, and carbon cycling in ecosystems [1–3]. Recently, global climate change and intense anthropogenic activities have led to alterations in lake hydrological systems, particularly in arid and semi-arid regions, inevitably affecting lakes' salinity [4–6]. Therefore, quantitative analysis of the climatic and anthropogenic drivers of lake salinity variation is essential for understanding response mechanisms and providing feedback on the climate by using lakes as climate indicator windows [7], aiding in both current and future lake management. However, conventional field measurement methods for lake salinity face challenges in conducting extensive and frequent data collection [8], which limits the ability to capture spatiotemporal patterns and explore the underlying drivers.

Remote sensing enables access to extensive information about salinity through the use of direct or indirect functions between radiance and salinity. Estimates of salinity using remote sensing can be based on microwave or optical data. While microwave-based salinity retrieval missions have been successful in oceanic studies, its spatial resolution of 40–150 km [9] is too coarse for inland lakes. Therefore, optical data with higher spatial resolution present an opportunity to estimate salinity in inland lakes. The present study utilized data from the Multi-Spectral Instrument (MSI) onboard Sentinel-2A/B (2015–present), a 12-bit push-broom sensor that measures in 13 spectral bands from visible to shortwave infrared, with spatial resolutions of 10 m, 20 m, and 60 m, and high revisit frequency of five days with twin satellites [10]. MSI-derived remote sensing reflectance $R_{rs}(\lambda)$ (units sr^{-1}) was used to monitor optically active constituents (OACs) or non-OACs [11–14]. However, deriving valid $R_{rs}(\lambda)$ requires a robust atmospheric correction specific to the atmospheric and aerosol conditions of the lake area [15,16].

Salinity is a non-OAC with no direct color signal and a complex non-linear relationship with $R_{rs}(\lambda)$ [17]. Given this complexity, machine learning (ML) algorithms may be used to explore the indirect relationship between reflected radiance and salinity by taking advantage of complex networks and structures. Several machine learning-based algorithms have been applied in inland lakes to estimate OACs and non-OACs, including multilayer perceptron neural networks (MPNNs) [18], extreme gradient boosting tree (XGB) [19], deep neural networks (DNNs) [20], convolutional neural networks (CNNs) [21], and random forest regression (RFR) [22]. For salinity applications, ML algorithms using the visible to near-infrared (NIR) bands have been used in single lakes or bays [23–25].

Inner Mongolia has a massive longitudinal gradient and the most pronounced wet and dry zonation of climate in China (Figure 1). Lake salinity extends over multiple orders of magnitude (Table 1), including freshwater (<1 g L^{-1}), brackish (1–3 g L^{-1}), and oligosaline (3–35 g L^{-1}). Many lakes receive large exogenous imports and have shown climatic effects that influence their salinity [26]. Runoff of rivers flowing into the lakes has seasonal variations, with concentrated precipitation in the summer with the flood season and increased runoff from melting snow in the spring with the temperatures rising. But some rivers dry up during the dry season. And the plume extends about 4–7 km in the summer, with an even wider range under wind effects. This study aimed to (1) develop a lake salinity retrieval model using MSI images through machine learning approaches, (2) employ the model to map spatiotemporal patterns of salinity in Inner Mongolian lakes, and (3) explore the drivers of lake salinity variation. The novelty of this study is to apply a singular approach across a range of lakes characterized by different drivers and conditions.

Table 1. Fundamental information about the sample lakes; not all parameters were measured, and the standard deviation is shown simply as S.D. in this study.

Lake Name	Sample Number	Salinity (ppt)		SDD (m)	
		Mean ± S.D.	Range (Min–Max)	Mean ± S.D.	Range (Min–Max)
Hulun	35	0.78 ± 0.08	0.54–0.86	0.29 ± 0.02	0.26–0.33
Dalinor	42	6.42 ± 0.16	6.15–6.60	0.48 ± 0.06	0.36–0.54
Chagannaoer	15	0.86 ± 0.03	0.83–0.92	/	/
Daihai	56	13.56 ± 2.38	10.67–16.81	2.37 ± 1.1	0.63–4.80
Hongjiannao	34	5.94 ± 0.13	5.82–6.30	1.78 ± 0.28	1.46–2.20
Nanhaizi	3	1.39 ± 0.01	1.39–1.41	0.27 ± 0.02	0.24–0.29
Ulansuhai	35	1.93 ± 0.64	0.86–3.27	0.88 ± 0.34	0.24–1.30
Juyan	11	4.61 ± 0.11	4.53–4.93	/	/

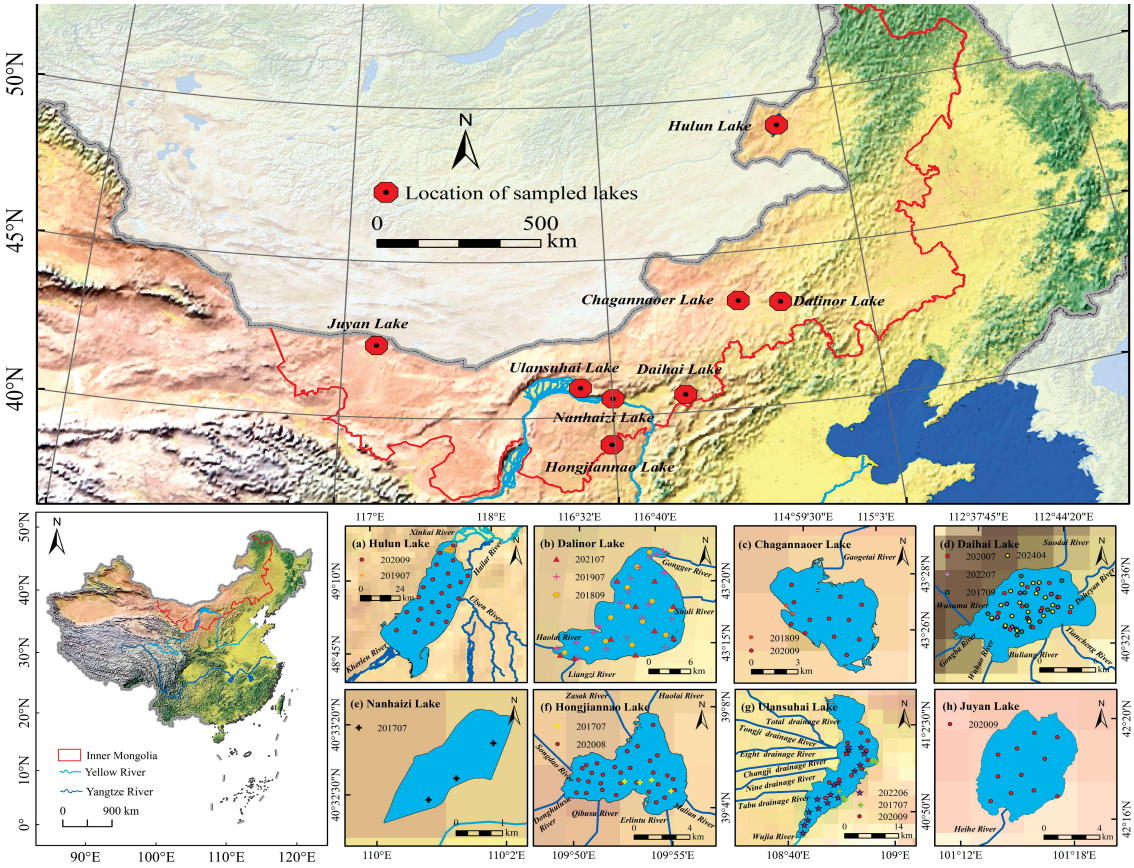

Figure 1. Location of the eight lakes and field samples, from east to west including (**a**–**h**) Hulun Lake, Dalinor Lake, Chagannaoer Lake, Daihai Lake, Nanhaizi Lake, Hongjiannao Lake, Ulansuhai Lake, and Juyan Lake; rivers colored light blue indicate outflow and dark blue means inflows.

2. Materials and Methods

2.1. Field Data

We obtained field data for the eight lakes through uniformly distributed in situ surveys and past studies (Table 1). A total of 231 data sources were used: 191 from in situ measurements and 40 from the published literature [27–29]. These data were divided into two datasets, Dataset one contains 211 field salinity data for model training and validation. Dataset two comprises 45 in situ measurements of the spectrum, absorption coefficients, chlorophyll-a (Chl-a), suspended particulate matter (SPM), and Secchi disk depth (SDD), which were employed to evaluate AC. Sampling and measurements were made within 6 h of the Sentinel-2 overpass (June 2022 of Ulansuhai, July 2022, and April 2024 of Daihai). Dataset one was of salinity only, with a matching interval of ±3 days between the in situ salinity and MSI images. Lake salinity does not change rapidly in the short term [30].

Salinity was measured in the spring, summer, and autumn by using a calibrated YSI multiparameter sonde (YSI, Inc., Yellow Springs, OH, USA). Above-water radiance measurements were carried out using the Spectral Evolution PSR-1100f (350–1050 nm, with 1 nm interval, Spectral Evolution, Inc., Haverhill, MA, USA), which measured in situ spectral data for the total water leaving radiance (L_{sw}), the sky radiance (L_{sky}), and the radiance of the reference gray panel (L_p) at a 135° azimuth relative to the sun and with a nadir viewing angle of 45° [31,32]. These radiances were used to calculate $R_{rs}(\lambda)$, and the equation is as follows:

$$R_{rs}(\lambda) = [(L_{sw} - \rho \times L_{sky}) \times \rho_p]/\pi \times L_p \quad (1)$$

where ρ is the air–water interface reflectance assumed to be 0.028 based on filed solar zenith angle, azimuth, and wind speed [31]. ρ_p is the reflectance of the gray panel of 30%. Finally, each band-center $R_{rs}(\lambda)$ was resampled using the spectral response function of Sentinel-2 A/B.

Surface water samples were collected in the field for laboratory analysis. Whatman GF/F filters were used to filter the water samples. Next, 90% acetone was used to extract the pigments for Chl-a concentration measurement with a Shimadzu UV2700 spectrophotometer (Shimadzu, Inc., Kyoto, Japan) [33]. SPM and suspended particulate inorganic matter (SPIM) were determined using gravimetric methods; the suspended particulate organic matter (SPOM) was associated with the difference between the SPM and the SPIM. Water clarity was measured using a Secchi disk. Absorption of the colored dissolved organic matter (CDOM), $[a_g(\lambda)]$, was measured using a UV2700 spectrophotometer with a spectral resolution of 1 nm from 280 to 700 nm after filtering [34].

2.2. Meteorological and Anthropogenic Factors

Temperature (°C), evaporation (mm), precipitation (mm), and wind speed (m/s) were obtained from ERA5-Land reanalysis data produced by the European Center for Medium-Range Weather Forecasts (ECMWF), with monthly data averaged by hour of day [35]. Monthly averaged meteorological data for eight lakes from 2016 to 2023 were obtained from ECMWF at a spatial resolution of 11 km. Annual data were based on averaged monthly data.

Three anthropogenic factors including population, nighttime light (nW/cm^2/sr), and normalized difference vegetation index (NDVI) were used to estimate the impact of human activities. The nighttime light and NDVI in lake basins with derived from Visible Infrared Imaging Radiometer Suite (VIIRS) and Landsat-8 imagers based on boundaries from the level-7 sub-basin in HydroBASINS [36] (Figure 2). Land use types of grassland dominate in most lake basins, but farmland types dominate in the Ulansuhai basin (data source: https://data.casearth.cn/, accessed on 10 October 2024). The proportion of impervious surfaces found in the Nanhaizi basin was 14%, which is higher than the other lake basins and indicates intensive socio-economic activities (Figure 2). The population data were collected from the statistical yearbook (https://tj.nmg.gov.cn/tjyw/, accessed on 1 July 2024). Annual anthropogenic data from 2016 to 2023 were used.

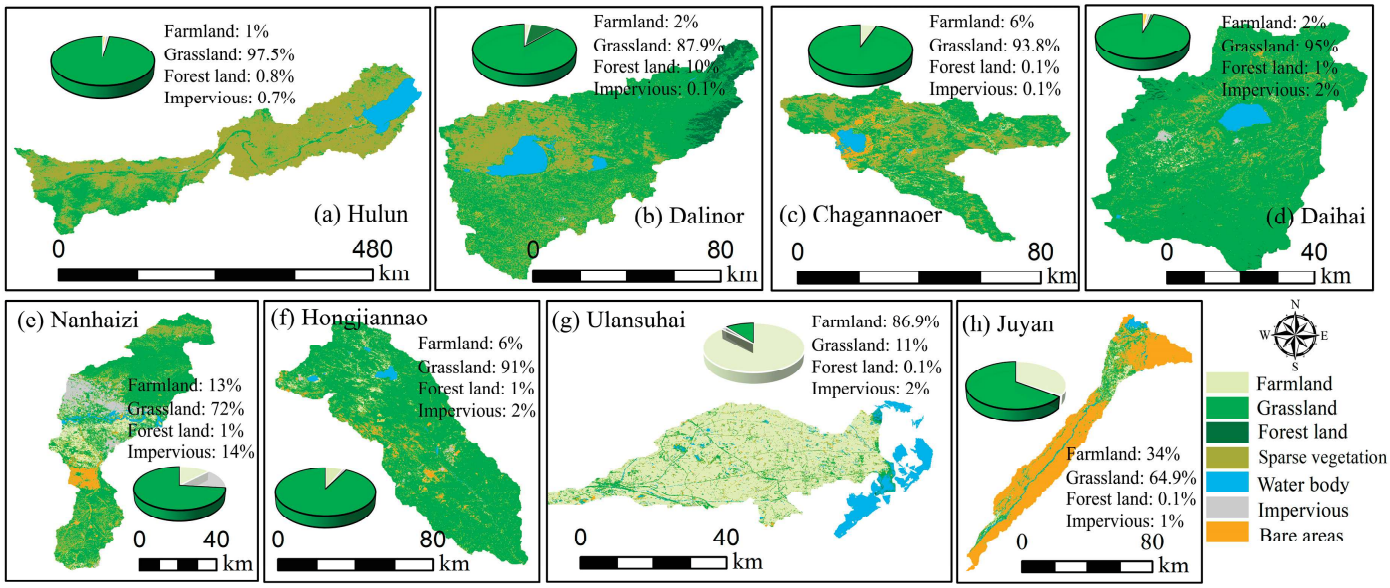

Figure 2. (**a**–**h**) The level-7 sub-basins of the corresponding lakes and seven types of land use, and the relative proportions of farmland, grassland, forest land, and impervious surfaces associated with human activity.

2.3. Sentinel-2 MSI Data and Preprocessing

2.3.1. Sentinel-2 MSI Data and Lake Area

A total of 485 Sentinel-2 MSI Level-1C images covering eight study lakes were downloaded from the Copernicus Data Space Ecosystem for the period from March 2016 to June 2024. The images for each year covered spring (March to May), summer (June to August), and autumn (September to November) under cloudless conditions. Winter lake conditions were dominated by ice cover. The lake area was extracted by using the Normalized Difference Water Index (NDWI) and the OTSU algorithm based on the Google Earth Engine (GEE) platform [37].

2.3.2. Atmospheric Correction

The optimal AC for the eight Inner Mongolian lakes was determined by comparing six AC algorithms: the Atmospheric Correction for OLI lite with Dark Spectrum Fitting algorithm (ACOLITE DSF) [38,39], the Case 2 Regional Coast Color (C2RCC) processor [40,41], the POLYnomial-based algorithm applied to MERIS (POLYMER) [42,43], the Management Unit of the North Seas Mathematical Model (MUMM) [44], the image CORrection for atmospheric effects (iCOR) [45], and the Sen2Cor [46]. With the exception of the iCOR (comprehensive processor) and Sen2Cor (designed for land), the other algorithms were designed for water processing. Each AC method primarily operated with default parameters, as detailed in Table S1. For AC algorithms that output water-leaving reflectance (p_w, dimensionless), the products were transformed to $R_{rs}(\lambda)$ by dividing by π. The six AC algorithms were evaluated based on 45 matched $R_{rs}(\lambda)$. These $R_{rs}(\lambda)$ images were resampled to 10 m spatial resolution.

2.4. Salinity Retrieval Model Training

MSI image-derived $R_{rs}(443)$, $R_{rs}(497)$, $R_{rs}(560)$, $R_{rs}(664)$, $R_{rs}(704)$, $R_{rs}(740)$, $R_{rs}(842)$, B4/(B4 + B3), B4/(B2 + B3), B4/B2, NDWI, chromaticity angle (alpha), and lake area were used as input features; more details about feature selection are provided in the Supporting Materials (Text S1). The 211 matched pairs of salinity and images were randomly divided into 70% training (N = 141) and 30% test datasets (N = 70), based on the size of Dataset one and the ratio commonly used for ML algorithms. The training dataset was used to determine the model parameters and structure, while the testing dataset was utilized for model validation. During training, a GridSearchSV method was used to search the model hyperparameters. Four ML methods were selected including XGB, CNN, DNN, and RFR. The XGB model is a powerful ensemble learner based on decision trees, which uses an additive strategy to integrate multiple trees [47]; through iterative fitting of the residuals until reaching the threshold, the sum of the predicted scores on the leaf nodes of each tree is the prediction. The mathematical structure is to determine the optimal objective function with loss and regularization terms, as follows:

$$\mathrm{obj} = \sum_{i=1}^{n} L(x_i, y_i) + \sum_{k=1}^{K} \Omega(f_k) \tag{2}$$

$$\Omega(f_k) = \gamma T + \frac{1}{2}\lambda \|\omega\|^2 \tag{3}$$

where i represents the i-th training data, n is the number of training data, $L(x_i, y_i)$ is the difference between measured (x_i) and estimated (y_i), $\Omega(f_k)$ is the complexity of the k-th tree, K is the number of trees, T is the number of leaves, γ and λ are the regularization coefficients, and ω is the leaf weight. In this study, we constructed the XGB salinity model as shown in Figure 3. Four model structures and hyperparameter settings are specified in Table S2.

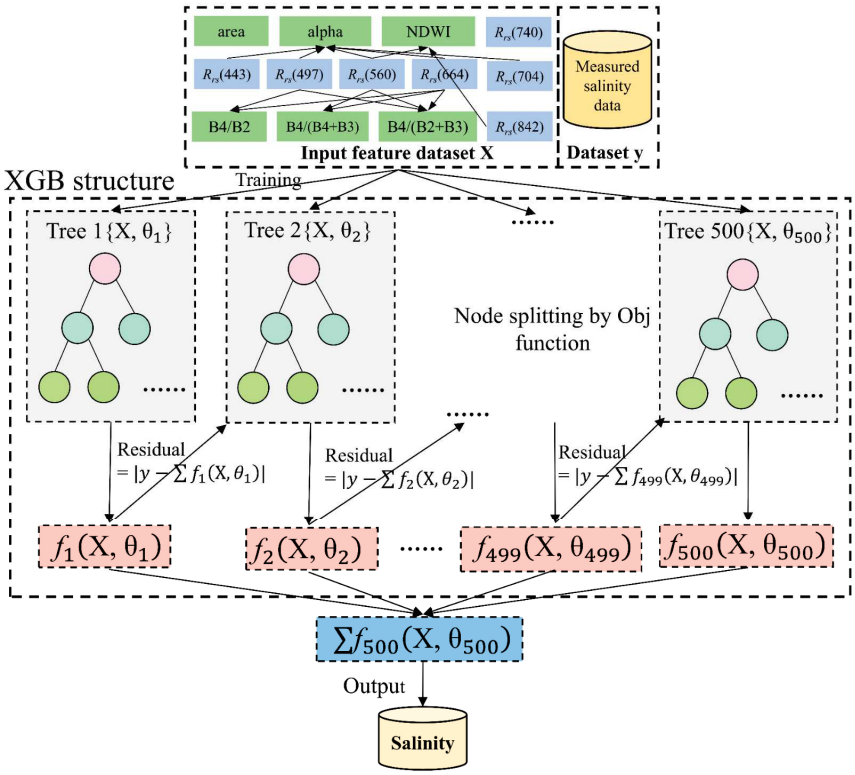

Figure 3. The fundamental structure of the XGB salinity model constructed in this research. Model inputs include the feature variable (X) and the target variable (y, measured salinity). During training, an initial learner (Tree 1) is first fit using the entire dataset; subsequently, a tree is added to fit the residual of the previous tree, and finally, the leaf node scores corresponding to the optimal objective function of each tree are summed to estimate salinity. θ represents the parameter corresponding to solving the optimal Obj for each tree.

To assess model stability and generalization performance, we performed the k-fold cross-validation (CV) procedure after determining the model's structure. This step enables one to obtain information about whether the model relies on the training dataset [48]. The entire dataset was randomly divided into five folds, with four sets used for training and one set for testing. These were repeated until the test set covered five folds, and the averaged statistical metrics of five evaluations were used to assess model performance. Finally, the optimal model was selected to map spatiotemporal patterns of water salinity in Inner Mongolian lakes using MSI images from 2016 to 2024. Subsequently, pixel-based annual and seasonal mean salinity were calculated for the eight lakes.

2.5. Driver Mining

A generalized linear model (GLM) was implemented to explore the relative importance of different drivers of the interannual and monthly changes in lake salinity for each lake. The coefficients of different variables in the linear model were interpreted as contribution values to understand the extent to which meteorological and anthropogenic factors influence salinity variation. Correlations between salinity and the driving factors were also investigated.

2.6. Trend Analysis

The Mann–Kendall test was applied to detect trends in annual average lake salinity from 2016 to 2024, with Sen's slope quantifying the monotonic change rate in salinity over the past nine years. This approach is more resistant to outliers and non-normal distributions than least-squares regression [49].

2.7. Accuracy Analysis

The accuracy of the estimated salinity values and $R_{rs}(\lambda)$ were analyzed using the coefficient of determination (R^2), root mean square error (RMSE), mean absolute error (MAE), mean absolute percentage error (MAPE), bias (systematic error), and percent of valid matched pairs (VP). These metrics' formulas are written as:

$$\mathrm{RMSE} = \sqrt{\frac{1}{N}\sum_{i=1}^{N}(y_i - x_i)^2} \tag{4}$$

$$\mathrm{MAE} = \frac{\sum_{i=1}^{N}|y_i - x_i|}{N} \tag{5}$$

$$\mathrm{MAPE} = \frac{1}{N}\sum_{i=1}^{N}\left|\frac{y_i - x_i}{x_i}\right| \times 100\% \tag{6}$$

$$\mathrm{bias} = 10^{\left(\frac{\sum_{i=1}^{N}\log_{10}y_i - \log_{10}x_i}{N}\right)} \tag{7}$$

$$\mathrm{VP} = \frac{n}{N} \times 100\% \tag{8}$$

where y and x are the estimated and measured values, i represents the i-th sampling data, n is the number of valid pairs, due to AC sometimes fails with abnormal values, N is the number of pairs.

2.8. Analysis Overview

This study consists of three main modules, shown in Figure 4. The first module is the collection of satellite data and field surveys. The second module is the AC of the MSI data and salinity model development with validation. The final module is the driver analysis of salinity variation using the GLM.

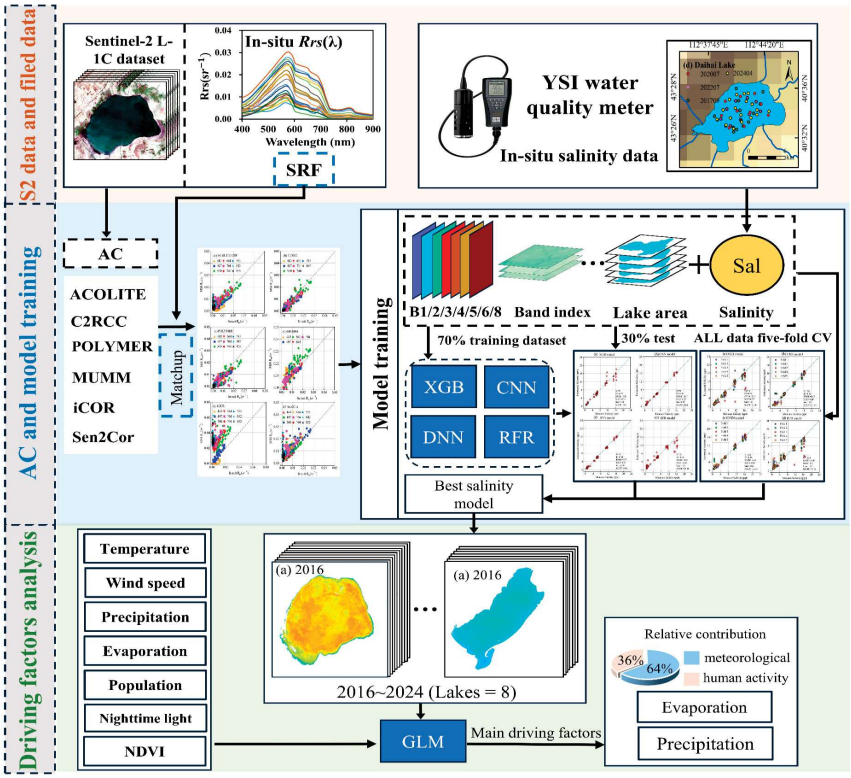

Figure 4. Overall framework for salinity retrieval and driving analysis.

3. Results

3.1. Performance of Atmospheric Correction Algorithms

The performance of the six AC algorithms showed relatively high accuracy in the green band (560 nm) and red band (664 and 704 nm) ($R^2 \geq 0.41$, RMSE ≤ 0.0255 sr^{-1}, VP $\geq 22.22\%$) but poor accuracy in the blue band (443 and 497 nm) and the NIR bands (842 and 865 nm). The ACOLITE and C2RCC outperformed the MUMM, POLYMER, and Sen2Cor, with iCOR performing worst (Table S3 and Figure 5). ACOLITE had the most valid pairs (VP $\geq 88.89\%$), while the C2RCC achieved the highest R^2 in each band ($R^2 \geq 0.33$). Both processors showed different strengths and required further analysis.

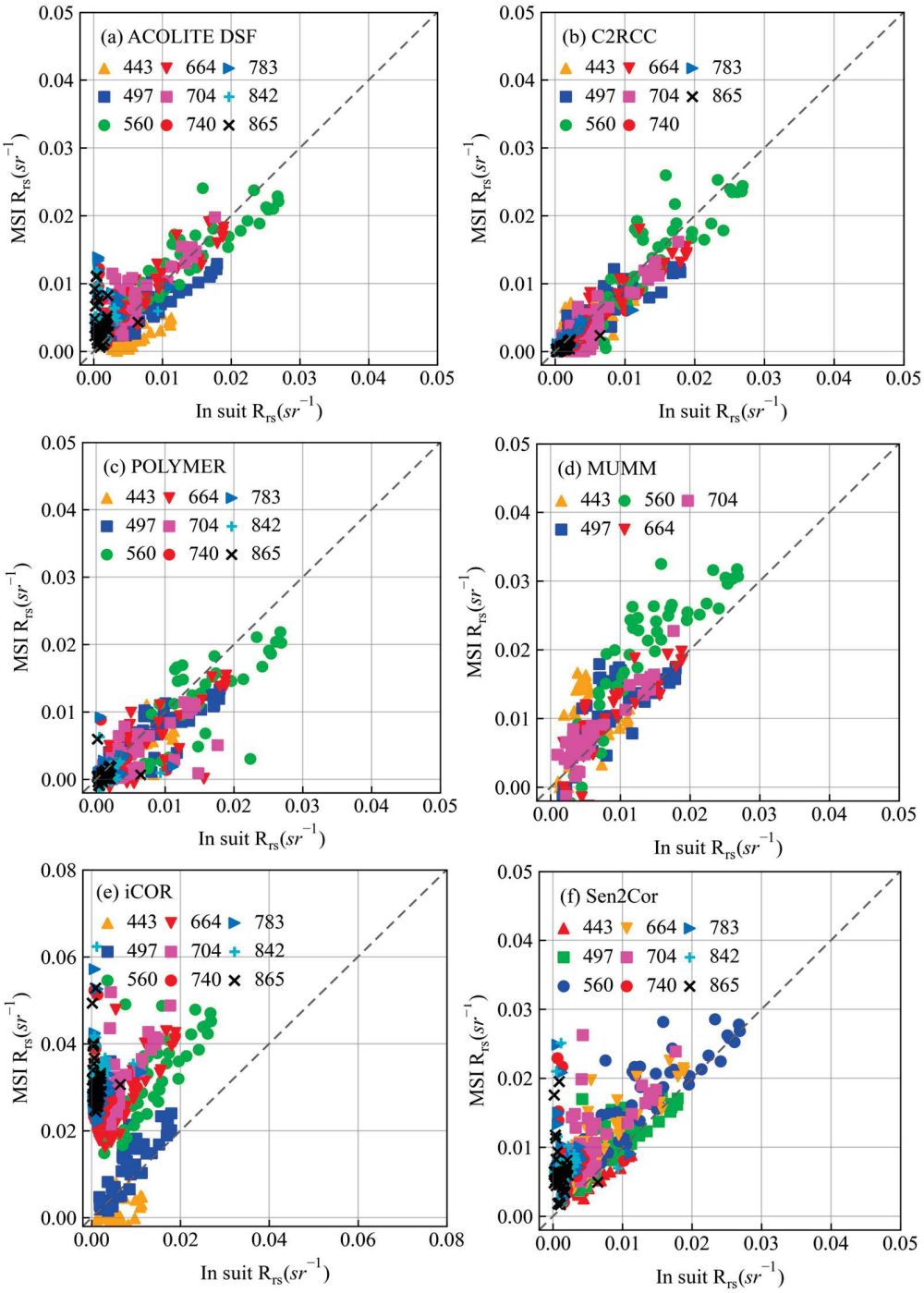

Figure 5. Scatterplot of in situ $R_{rs}(\lambda)$ and MSI image-derived $R_{rs}(\lambda)$ using (**a**) ACOLITE DSF, (**b**) C2RCC, (**c**) PLYMER, (**d**) MUMM, (**e**) iCOR, and (**f**) Sen2Cor.

The $R_{rs}(\lambda)$ spectral shape of the ACOLITE and C2RCC was compared in waters with and without aquatic vegetation (submerged and floating) (Figure 6), using 5 × 5 10 m pixels centered around the in situ station to explore changes in spectral shape [50]. The averaged $R_{rs}(\lambda)$ retrieved from C2RCC and ACOLITE in waters without aquatic plants provided similar and consistent trends with averaged in situ $R_{rs}(\lambda)$ (Figure 6b). For sites with aquatic vegetation, C2RCC failed in the 443–704 nm range (red box in Figure 6e) and did not generate spectral shapes that were similar to the in situ measurements. ACOLITE reproduced the correct spectral shape with high reflectance at 740–865 nm (Figure 6d). ACOLITE was then used to process the MSI images in this study.

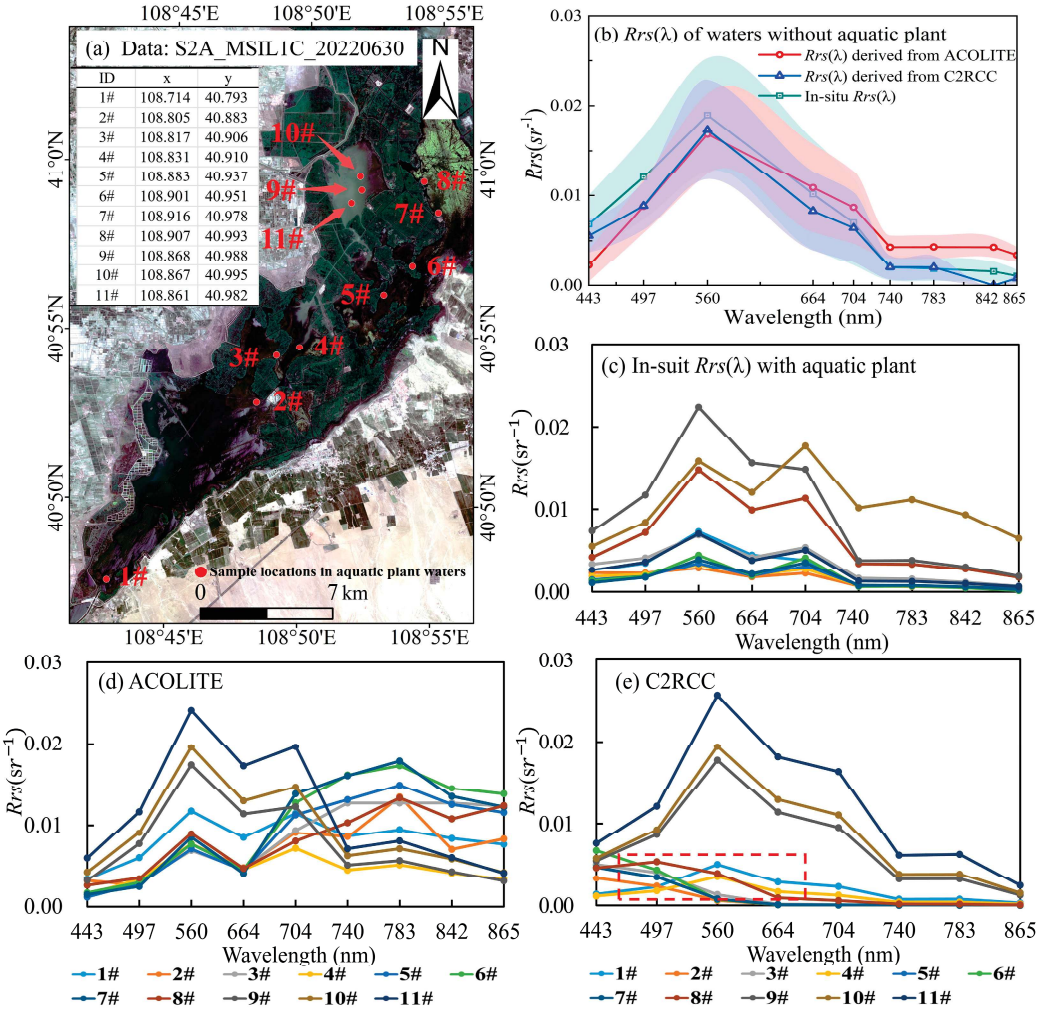

Figure 6. (**a**) Sample locations in aquatic plant waters and coordinates, (**b**) averaged $R_{rs}(\lambda)$ in situ, ACOLITE and C2RCC, respectively, in waters without aquatic plants, (**c**) in situ $R_{rs}(\lambda)$ with aquatic plants, (**d**) ACOLITE-derived $R_{rs}(\lambda)$ from MSI images in aquatic plant waters, and (**e**) C2RCC output $R_{rs}(\lambda)$ in aquatic plant waters.

The accuracy of ACOLITE-derived $R_{rs}(\lambda)$ from MSI images affects the performance of the XGB model. The ACOLITE processor had high accuracy at 497–740 nm (RMSE < 0.0038 sr^{-1}) but performed worse at 783–865 nm (RMSE > 0.0039 sr^{-1}) (Table S3), where errors propagate to the model, affecting its accuracy. Overestimates of aerosol optical thickness occur when the calibration window does not contain dark pixels, which may overcorrect and result in negative values [51], causing an underestimate of salinity. The low observational viewing angles of Sentinel-2 make the images susceptible to sunglint, although the dark spectrum fitting algorithms reduce the effect of sunglint to some extent but do not eliminate it [52]. Adjacency effects and

bottom reflections can lead to incorrect estimates of salinity in the nearshore waters of lakes. To minimize these effects, a water mask with two pixels indentation was used for cropping [53].

3.2. Model Performance

To select the optimal machine learning approach for salinity retrieval, scatterplots of the 30% independent dataset test and five-fold CV were plotted; the performance of the four models is shown in Figure 7a,b and Table S4. From the results of the 30% dataset test (N = 70), the XGB model estimated salinity with a wider range (0.72–18.1 ppt) (Figure 7a), whereas the CNN, DNN, and RFR tended to underestimate salinity with a narrower range (0.74–15.75 ppt) (Figure 7c–h). The XGB model had high accuracy (R2 = 0.98; RMSE = 1.03 ppt; MAE = 0.53 ppt; MAPE = 9.95 %); it slightly overestimated salinity in the range of 10–18 ppt but generally on the 1:1 line (Figure 7a).

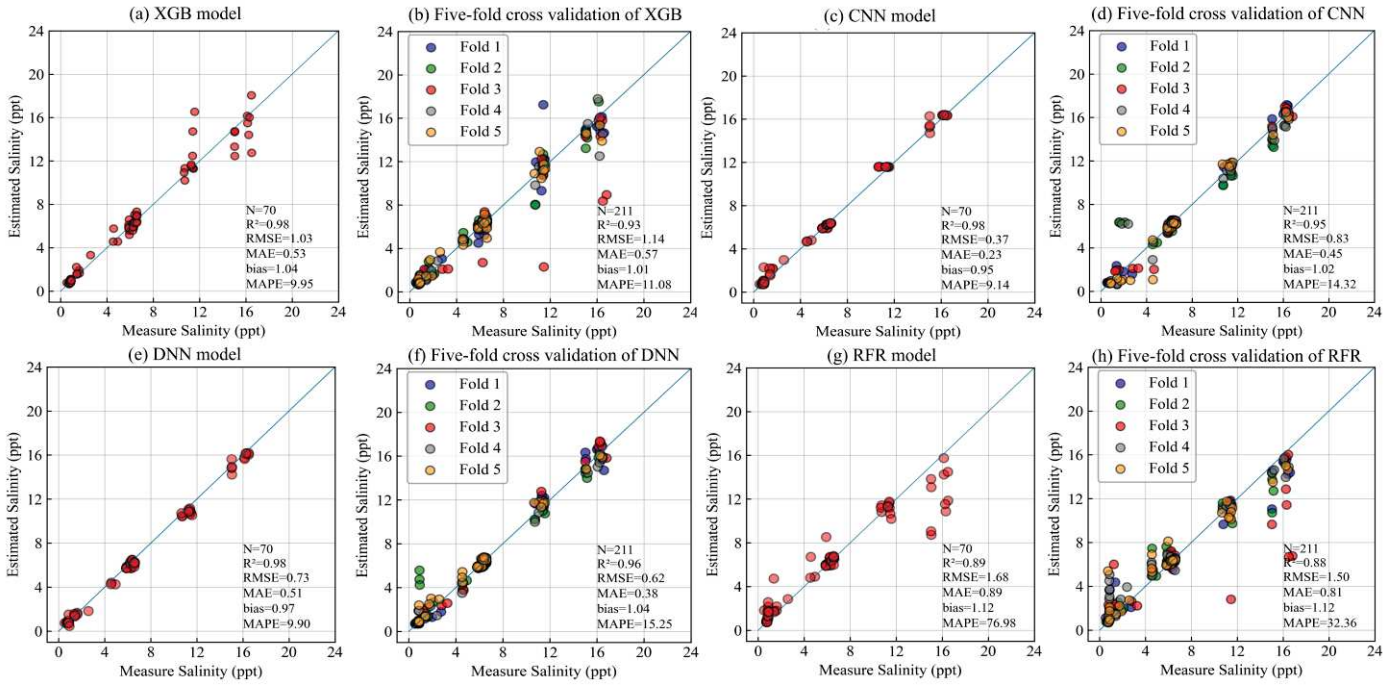

Figure 7. (**a**–**h**) Scatterplot of measured salinity versus estimated salinity from the 30% independent test and five-fold cross-validation of the four models.

The five-fold CV of the four ML models suggests that each model has acceptable performance (N = 211) (Figure 7). The XGB model performs better than the CNN and DNN, with RFR as the worst. The MAPE and bias of the CNN and DNN models were greater than those of the XGB model due to these models having deficiencies in stability (Figure 7d,f). The XGB model had a mean bias of 1.01 and a MAPE of 11.08%, which was closest to the results of the 30% dataset test (Figure 7a). Moreover, the salinity derived from the five-fold CV of the XGB model was consistent with the distribution range of measured salinity, demonstrating its robustness with unremarkable reliance on the training dataset. Consequently, the optimal XGB salinity model was selected by comprehensively assessing its performance during the 30% dataset test and the five-fold CV of each model, applied to generate long-term salinity data.

3.3. Spatial Pattern of Lake Salinity

The seasonal salinity maps of the eight lakes show the highest mean salinity during the autumn (4.53 ppt) and spring (4.43 ppt) compared to the summer (4.08 ppt). Seasonal salinity variation was greatest in Daihai Lake, with a minimum value of 10.98 ± 1.47 ppt in the spring and a maximum value of 12.99 ± 0.91 ppt in the autumn (Figure 8v–x). Hulun Lake had the smallest seasonal salinity variation, with a minimum value of 1.01 ± 0.07 ppt

during the autumn and a maximum value of 1.35 ± 0.13 ppt during the spring (Figure 8d–f). The spatial distribution of lake salinity showed the lowest values at the river inlet during summer-related freshwater plume in the southern sections of Hulun Lake and Juyan Lake (Figure 8e,t). The Daihai, Dalinor, Hongjiannao, and Nanhaizi lakes exhibited gradually increasing salinity from the shores to the center in all seasons. Ulansuhai Lake exhibited higher salinity in the southern region than the in northern region in all seasons. Chagannaoer Lake did not show significant spatial variations in salinity.

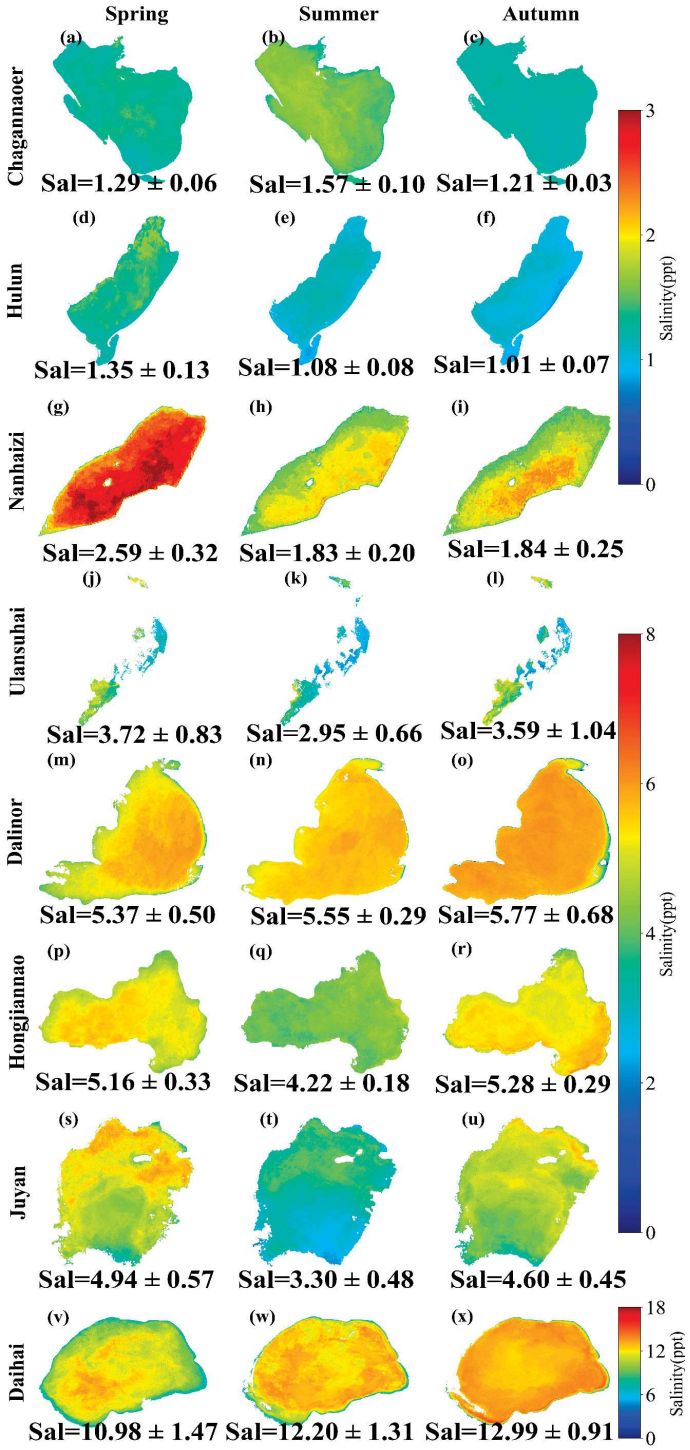

Figure 8. (**a**–**x**) Seasonal average salinity (mean ± S.D., with salinity simply as Sal) from 2016 to 2024 in the eight lakes derived from MSI images by implementing the XGB model. Missing winter data due to ice cover.

Annual scale salinity maps showed interannual spatial variations (Figure 9), prominent in oligosaline lakes (Figure 9). The Dalinor, Hongjiannao, and Daihai lakes exhibited uniform and homogeneous high salinity patches in the lake centers and low salinity at the lake edges each year. The salinity of Juyan Lake shows a spatial pattern of low south and high north from 2016 to 2024, as shown in Figure 9(7a–7i). Ulansuhai Lake had minor interannual changes in the north-south pattern. There were no significant interannual spatial variations of salinity in the Chagannaoer and Hulun lakes, with an interannual difference of less than 0.6 ppt.

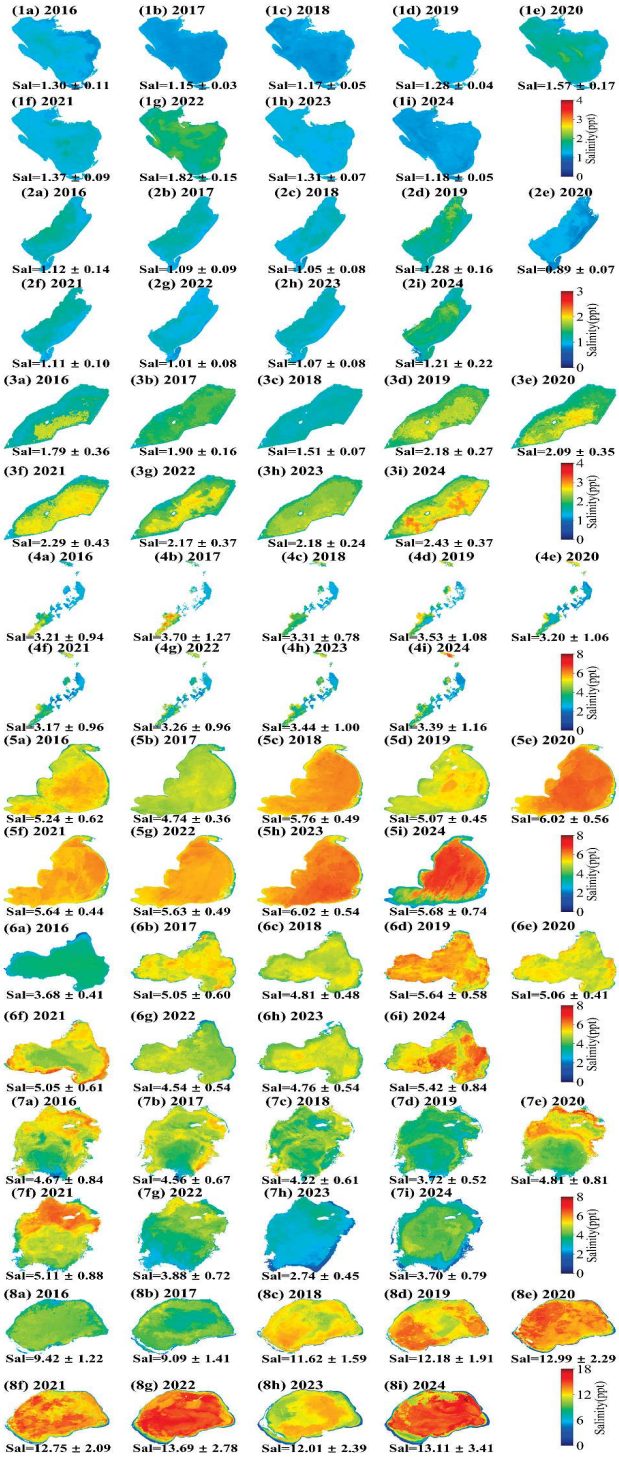

Figure 9. (**1a**–**8i**) Annual average salinity (mean ± S.D.) from 2016 to 2024 in the eight lakes derived from MSI images by employing the XGB salinity model.

3.4. Interannual Trends in Lake Salinity

From 2016 to 2024, two lakes had a positive trend in salinity, with most lakes showing non-significant changes (Figure 10). The salinity in Daihai (change rate: 0.57 ppt/year, $p < 0.05$) and Nanhaizi (0.11 ppt/year, $p < 0.05$) was positive. Trends were not significant in Hongjiannao (0.12 ppt/year, $p = 0.28$), Chagannaoer (0.01 ppt/year, $p = 0.72$), Dalinor (0.13 ppt/year, $p = 0.07$), Juyan (−0.19 ppt/year, $p = 0.13$), Ulansuhai (−0.01 ppt/year, $p = 0.73$), and Hulun (−0.01 ppt/year, $p = 0.95$).

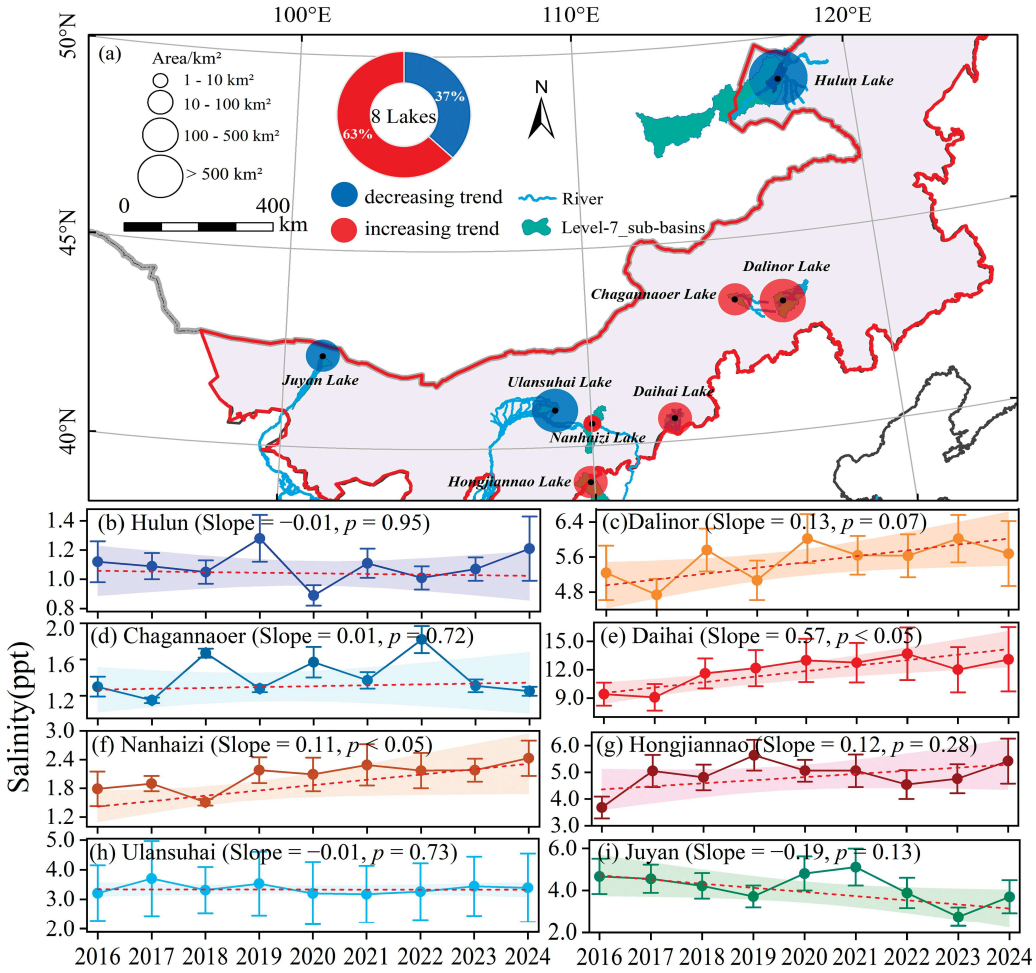

Figure 10. (**a**) Spatial distribution of lakes and proportions with interannual salinity increase or decrease and (**b**–**i**) annual average salinity changes from 2016 to 2024 in the eight lakes.

3.5. Driving Factors of Lake Salinity Variations

Interannual and seasonal salinity variations in the eight lakes were compared to coincident climate and anthropogenic factors using a GLM modeling approach. There were seven drivers considered: temperature, wind speed, precipitation, evaporation, population, nighttime light, and the NDVI (Figure 11a–p). In terms of interannual drivers for all lakes together (Figure 11a–h), climate-related factors were the dominant drivers of salinity change in most lakes. The relative contributions of anthropogenic factors exceeded climate factors in Nanhaizi Lake and Hongjiannao Lake (Figure 11e,f). Interestingly, temperature exhibited a relatively minor contribution to interannual and seasonal salinity variations, particularly at the seasonal scale.

At an annual scale (Figure 11a–h), evaporation and precipitation were the most important climate-related drivers, with the averaged relative contributions of 26% and 20% across all lakes. Evaporation controlled salinity changes in Dalinor Lake with a relative contribution of 50.5%. Precipitation dominated changes in Juyan Lake with a relative

contribution of 52.2%. The interannual salinity dynamics of the Daihai and Ulansuhai lakes were controlled by a combination of wind speed, precipitation, and evaporation.

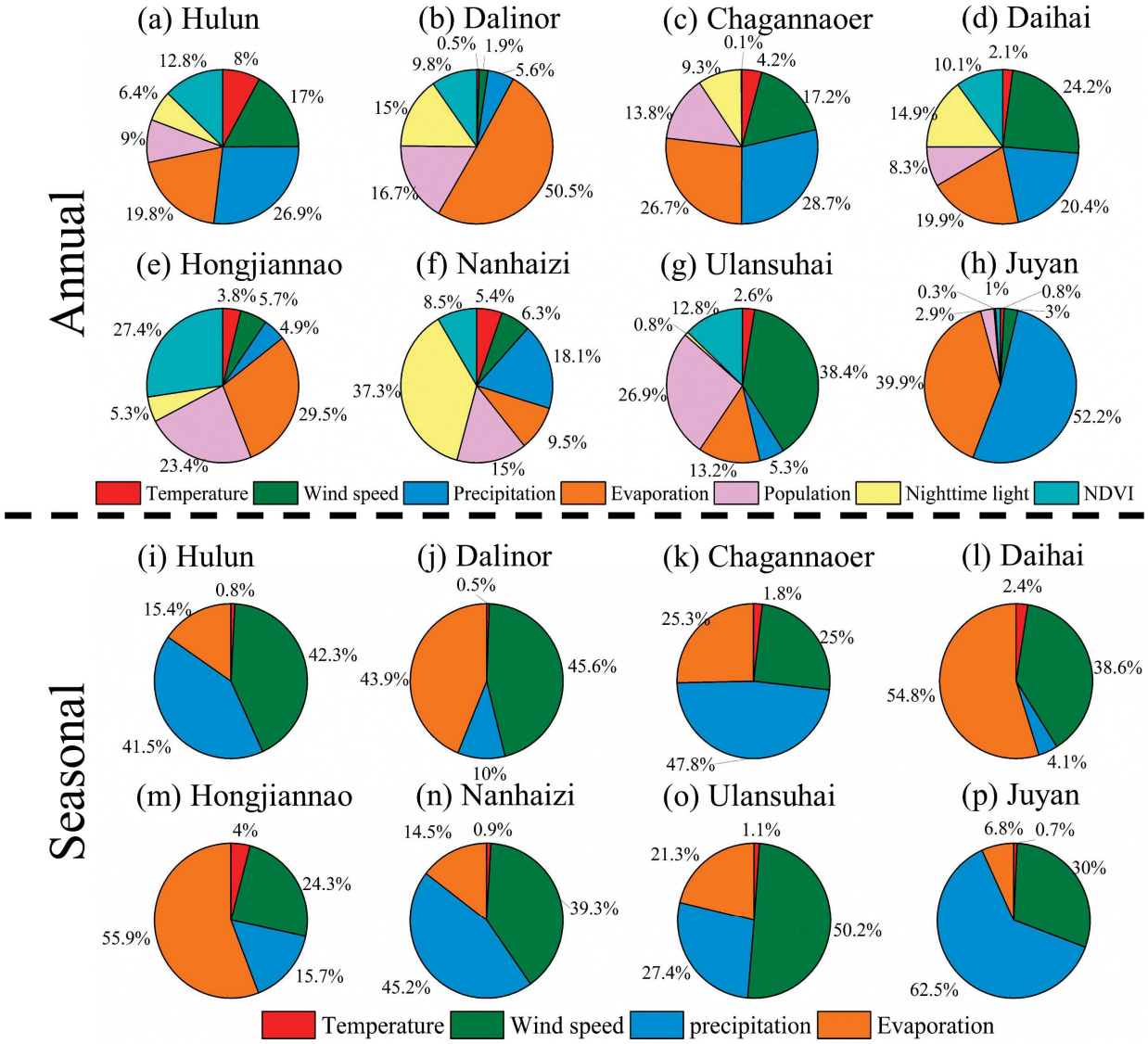

Figure 11. Relative contributions of drivers of salinity change in the eight lakes. (**a**–**h**) Annual scale relative contributions of meteorological and anthropogenic factors and (**i**–**p**) seasonal scale relative contributions of meteorological factors.

At the seasonal scale (Figure 11i–p), precipitation dominated salinity changes in the Hulun, Chagannaoer, Juyan, and Nanhaizi lakes with relative contributions of 41%, 48%, 45%, and 63%, respectively. Evaporation dominated in the Hongjiannao and Dalinor lakes. In Ulansuhai Lake, wind speed had the largest relative contribution (50%). Evaporation and precipitation jointly controlled the seasonal salinity dynamics in Daihai Lake.

Correlations between salinity variations with drivers further confirm the importance of climate-related drivers (Figure 12a–d). Regarding the correlations at interannual scales ($p < 0.05$) (Figure 12a,b), salinity in the Hongjiannao and Nanhaizi lakes showed negative correlations with precipitation ($|r| < 0.83$), while the salinity of Ulansuhai Lake increased with temperature ($r = 0.64$). But the salinity in Daihai Lake presented positive correlations with nighttime light ($r = 0.77$). At the seasonal scale ($p < 0.05$) (Figure 12c,d), temperature, evaporation, and precipitation showed negative correlations ($|r| < 0.79$) with salinity in the Juyan, Ulansuhai, and Hongjiannao lakes. For salinity, temperature and evaporation presented positive correlations in Chagannaoer Lake ($r > 0.39$).

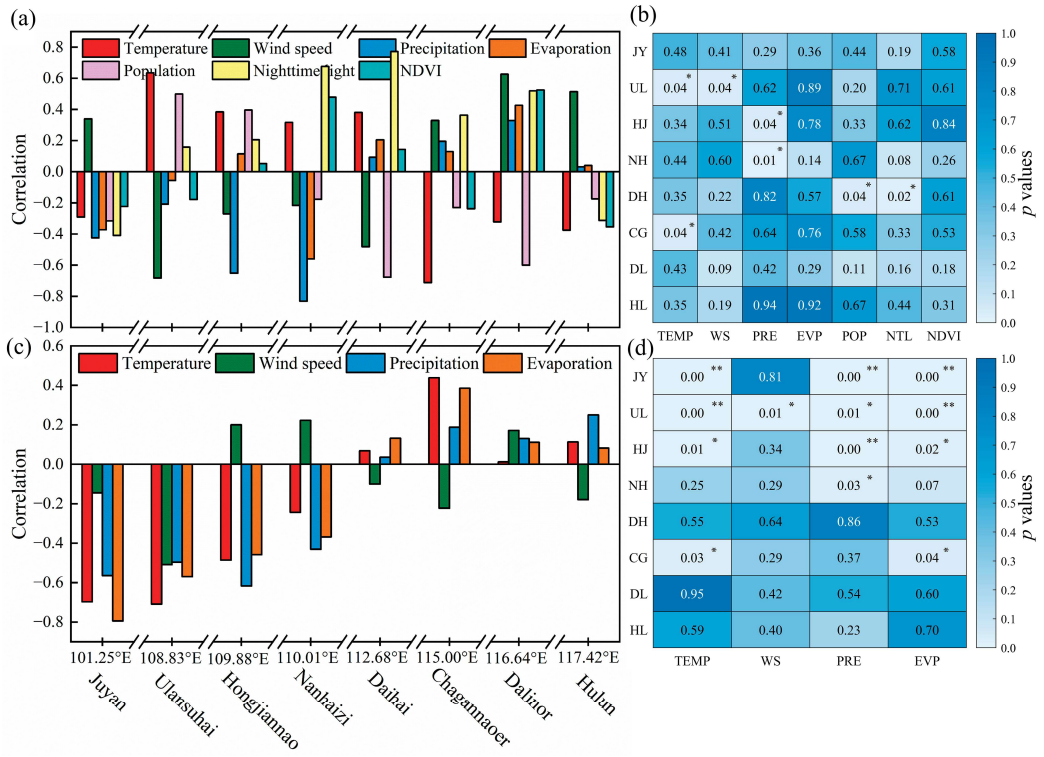

Figure 12. (**a**) Correlation between annual average salinity and meteorological factors with anthropogenic drivers; (**b**) *p*-values of annual driving factors and temperature, wind speed, precipitation, evaporation, population, and nighttime light abbreviated as TEMP, WS, PRE, EVP, POP, and NTL; (**c**) correlation between seasonal average salinity and meteorological drivers; (**d**) *p*-values of seasonal drivers. Horizontal coordinates are the central longitude of each lake. The lakes from Juyan Lake to Hulun Lake are simply noted as JY, UL, NHZ, DH, CG, DL, and HL, respectively. * and ** denote significant correlation at $p < 0.05$ and 0.01.

4. Discussion

4.1. Model Interpretation: Capabilities and Limitations

The XGB algorithm performed well for the eight lakes, generating a valid salinity time series. It has been previously shown that salinity can be established as a function of $a_g(\lambda)$ or SDD, both optical characteristics that can be estimated by remote sensing [54,55]. However, this indirect method is inherently complex and strongly conditioned by the accuracy of the parameter associating salinity with $a_g(\lambda)$, for example. Likewise, $a_g(\lambda)$ and SDD are strongly influenced by Chl-a and SPM. The XGB model relating $R_{rs}(\lambda)$ to salinity reduces the effect of error propagation on the predictions. With respect to other machine learning approaches, the XGB algorithm outperformed neural network models without overfitting, which occurred in the CNN and DNN approaches (Figure 7c–f), due to design regularization to control overfitting and implement gradient descent of the residuals using an optimization strategy [47]. Another tree model approach, RFR, performed poorly (with a much higher MAPE) compared to XGB, as it did not incorporate the covariance of input features and also lacked regularization.

Interestingly, XGB reached the highest scores at the red edge (740 nm) (Figure S1), suggesting that 740 nm was the most sensitive band for salinity retrieval. This result supports earlier studies that suggest that the red and NIR bands are most sensitive to salinity changes [56]. The green (560 nm) and blue bands (443 and 497 nm) have also been used for salinity estimates [24]. They showed some sensitivity in the present study. As previously hypothesized [57], the results suggest that, as salinity increases, a change in absorption occurs, and the maximum wavelengths reflect a shift to higher wavelengths. Thus, multiple bands from visible to NIR can be used as inputs to explore salinity changes [23,25]. Lake

area was also an important component of the XGB model, indicating a relationship between the bathymetric features of a lake and its salinity [5].

Similarly, for all machine learning models, the application of the XGB model is dependent on the training datasets used. This study included salinity values spanning three magnitudes but lacked samples from hypersaline lakes (>35 g L^{-1}), making the model inappropriate for high-salinity lakes. It should also be noted that spatiotemporal heterogeneity caused by in situ salinity within three days of the satellite overpass would inevitably induce errors in the model estimations. The ACOLITE algorithm showed satisfactory accuracy in the visible and NIR bands, which helped to improve the performance of the XGB model. But the influence of sunglint and adjacency effects was not completely eliminated and might cause uncertainty of salinity values in nearshore water pixels.

4.2. Mechanism Analysis of Salinity Driving Factors

Investigation of salinity drivers demonstrated that precipitation and evaporation play key roles in lake salinity variations (Figure 11), which influence salinity by controlling the water volume balance in the lake; these results reflect similar findings on salinity variations in Bosten Lake [58,59]. Precipitation supplements surface runoff injections into lakes, diluting salinity as total dissolved solids dissolve more solvents, which explains the negative correlation of salinity with precipitation exhibited in most lakes on both interannual and seasonal scales (Figure 12a,c). Salinity displayed negative correlations with temperature and evaporation on a seasonal scale, likely also related to summer precipitation [60]. A few lakes present a positive mode between salinity and precipitation; this pattern can be ascribed to anthropogenic activities that have substantially intercepted runoff, causing water volume decline combined with runoff from agricultural areas containing nutrients and salts [61]. Wind speed exhibits a high relative contribution to salinity in several lakes (Figure 11), as wind can accelerate the diffusion of ions by altering the hydrodynamic field [62]. Note that temperature exhibited a minor contribution to salinity dynamics; a possible interpretation was that the increased precipitation and freshwater inflow during the summer diluted the salinity, thereby masking the effect of temperature [63]. In addition, lake salinity was compared between early and late spring after ice melt, indicating that salinity often decreases, likely as a result of increased solvents from ice melt or spring flooding (Figure 13).

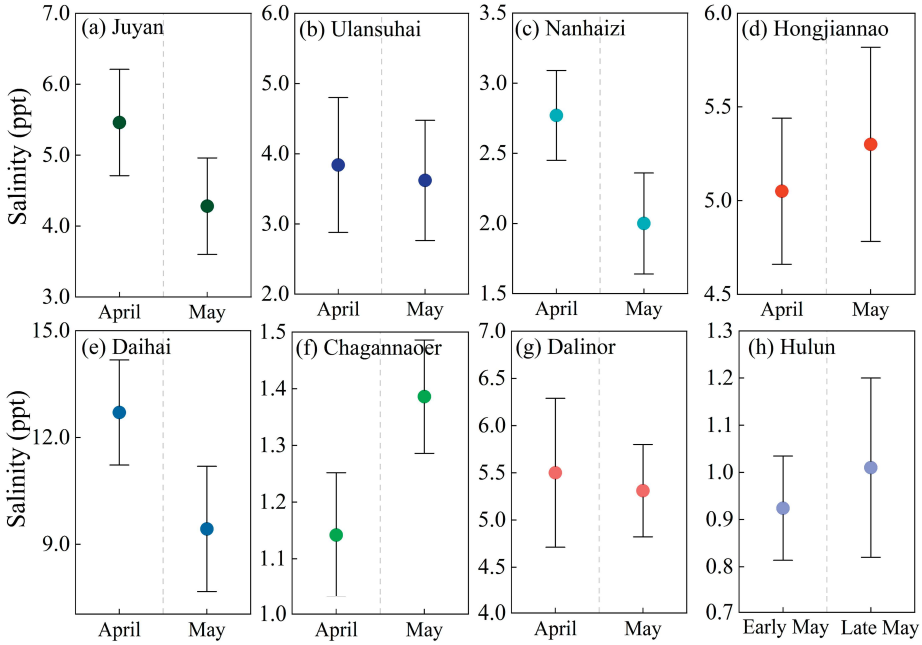

Figure 13. (**a**–**h**) Comparison of the salinity of the eight lakes in the early and late spring after ice melt; most lakes had melted ice in April, but Hulun Lake had melted ice in May.

The responses of salinity under human activities cannot be ignored. The contributions of anthropogenic factors exceeded climatic factors in the Hongjiannao and Nanhaizi lakes (Figure 11e,f). This is likely due to the higher population and more pronounced economic activities in these two drainage basins [64]. A significant positive correlation between salinity and nighttime light was observed in Daihai Lake (Figure 12a,b), indicating that intensive anthropogenic activities in the watershed tend to drive salinity increases. Especially in terminal lakes with long water renewal cycles, salinity responds sensitively to human activities [5].

4.3. Implications for Monitoring Salinity

Over recent decades, increases in lake salinity have occurred in lakes around the world, such as the Aral Sea in Central Asia [65], Urmia Lake [24], Great Salt Lake in the United States [66], and Daihai Lake in China [67]. Some lakes have shown decreased salinity, such as lakes on the Tibetan Plateau [5,55]. In the cold and arid Inner Mongolia region, lakes showed both trends and important interannual and seasonal changes, which could impact the microbial communities' species richness and functional diversity [2,68], as well as degrading habitat quality with potential losses such as species extinction if the biological tolerance thresholds are exceeded [69]. Additionally, increased salinity can reduce lake methane concentrations with consequent benefits for greenhouse gas emissions [70] and the lake carbon cycle [3]. Fortunately, high-resolution satellite images offer opportunities for the long-term monitoring of salinity variations. It is important to understand the basic condition of water quality and salinity trends through long-term monitoring and provide services for the routine management and restoration assessment of lakes in northern China.

The United Nations Sustainable Development Goal 6.3, specifically indicator 6.3.2, addresses the evaluation of water quality, proposed conductivity, or salinity as the key parameter for water quality monitoring [71]. However, there are significant data gaps that have limited the capacity of many countries to report data [72]. A global-based XGB salinity model could provide important new information on lake water quality, utilizing multi-source satellite data (terrestrial, water color, and microwave sensor products) coupled with field data to achieve broader salinity monitoring for SDG 6.3.

5. Conclusions

Through the determination of lake salinity using Sentinel-2 images coupled with a machine learning algorithm, seasonal and interannual variations were explored, along with an examination of potential drivers of salinity change over time. Average salinities in the autumn (4.53 ppt) and spring (4.43 ppt) were higher than in the summer (4.08 ppt), with the salinity diluted by freshwater inflows during the summer. The higher salinities were commonly observed in the lake center and tended to be consistent and homogeneous. Significant increase trends were found in Daihai Lake, dominated by a combination of wind speed, precipitation, and evaporation, and also in Nanhaizi Lake, controlled by human factors such as nighttime light. Meteorological factors are the primary drivers, with mean contributions of 64%, exceeding 36% for anthropogenic factors, with evaporation and precipitation as the key factors. The dilution of salinity by summer precipitation explains its negative correlation with temperature and evaporation, while potentially masking the contribution of temperature. The influence of human factors cannot be overlooked, especially in lakes with intense human activity within the watershed. Long-term monitoring of salinity using satellites enhances managerial staff's understanding of water salinization or desalination and safeguards lake ecosystem security.

Supplementary Materials: The following supporting information can be downloaded at: https://www.mdpi.com/article/10.3390/rs16203881/s1. Text S1: Input feature selection; Figure S1: Feature importance score of (a) RFR and (b) XGB; Table S1: Software version and parameter settings for each atmospheric correction processor; Table S2: Four machine learning model structures and hyperparameter settings; Table S3: Accuracy statistics of in situ measurements Rrs(λ) and six AC

processors derived MSI Rrs(λ); Table S4: Results of 30% independent dataset testing and five-fold cross-validation of four model.

Author Contributions: Conceptualization, M.D.; methodology, M.D. and Z.C.; validation, M.D.; data curation, R.M., L.W. and G.G.; writing—original draft, M.D.; writing—review and editing, M.D., R.M., S.A.L., M.H. and K.X.; supervision, R.M. and C.L.; funding acquisition, R.M. All authors have read and agreed to the published version of the manuscript.

Funding: This research was funded by the National Natural Science Foundation of China (Grant No. 42361144002 and No. 42371371).

Data Availability Statement: The raw data supporting the conclusions of this article will be made available by the authors upon request.

Acknowledgments: The authors thank Chuanmin Hu (University of South Florida) for providing valuable suggestions and their colleagues from NIGLAS (Zhengyang Yu, Yiqiu Wu, and Feizhou Cheng) and Inner Mongolia University for their help with the field measurements. We acknowledge data support from the Lake-Watershed Science Data Center (http://lake.geodata.cn, accessed on 7 October 2023).

Conflicts of Interest: The authors declare no conflicts of interest.

References

1. Jeppesen, E.; Beklioglu, M.; Ozkan, K.; Akyurek, Z. Salinization Increase Due to Climate Change Will Have Substantial Negative Effects on Inland Waters: A Call for Multifaceted Research at the Local and Global Scale. *Innovation* **2020**, *1*, 100030. [CrossRef] [PubMed]
2. Liu, C.; Wu, F.; Jiang, X.; Hu, Y.; Shao, K.; Tang, X.; Qin, B.; Gao, G. Salinity Is a Key Determinant for the Microeukaryotic Community in Lake Ecosystems of the Inner Mongolia Plateau, China. *Front. Microbiol.* **2022**, *13*, 841686. [CrossRef] [PubMed]
3. Liao, Y.; Xiao, Q.; Li, Y.; Yang, C.; Li, J.; Duan, H. Salinity Is an Important Factor in Carbon Emissions from an Inland Lake in Arid Region. *Sci. Total Environ.* **2024**, *906*, 167721. [CrossRef] [PubMed]
4. Ho, L.T.; Goethals, P.L.M. Opportunities and Challenges for the Sustainability of Lakes and Reservoirs in Relation to the Sustainable Development Goals (SDGs). *Water* **2019**, *11*, 1462. [CrossRef]
5. Song, C.; Luo, S.; Liu, K.; Chen, T.; Zhang, P.; Fan, C. Widespread Declines in Water Salinity of the Endorheic Tibetan Plateau Lakes. *Environ. Res. Commun.* **2022**, *4*, 091002. [CrossRef]
6. IPCC. *Climate Change 2023: Synthesis Report*; IPCC: Geneva, Switzerland, 2023.
7. Wang, X.; Yang, Y.; Wan, J.; Chen, Z.; Wang, N.; Guo, Y.; Wang, Y. Water Quality Variation and Driving Factors Quantitatively Evaluation of Urban Lakes during Quick Socioeconomic Development. *J. Environ. Manag.* **2023**, *344*, 118615. [CrossRef]
8. Ren, X.; Yu, R.; Liu, X.; Sun, H.; Yue, G.; Qi, Z.; Zhang, Z.; Li, X.; Wang, J.; Zhu, P.; et al. Spatial Changes and Driving Factors of Lake Water Quality in Inner Mongolia, China. *J. Arid Land* **2023**, *15*, 164–179. [CrossRef]
9. Reul, N.; Grodsky, S.A.; Arias, M.; Boutin, J.; Catany, R.; Chapron, B.; D'Amico, F.; Dinnat, E.; Donlon, C.; Fore, A.; et al. Sea Surface Salinity Estimates from Spaceborne L-Band Radiometers: An Overview of the First Decade of Observation (2010–2019). *Remote Sens. Environ.* **2020**, *242*, 111769. [CrossRef]
10. Drusch, M.; Del Bello, U.; Carlier, S.; Colin, O.; Fernandez, V.; Gascon, F.; Hoersch, B.; Isola, C.; Laberinti, P.; Martimort, P.; et al. Sentinel-2: ESA's Optical High-Resolution Mission for GMES Operational Services. *Remote Sens. Environ.* **2012**, *120*, 25–36. [CrossRef]
11. Toming, K.; Kutser, T.; Laas, A.; Sepp, M.; Paavel, B.; Noges, T. First Experiences in Mapping Lake Water Quality Parameters with Sentinel-2 MSI Imagery. *Remote Sens.* **2016**, *8*, 640. [CrossRef]
12. Pahlevan, N.; Sarkar, S.; Franz, B.A.; Balasubramanian, S.V.; He, J. Sentinel-2 MultiSpectral Instrument (MSI) Data Processing for Aquatic Science Applications: Demonstrations and Validations. *Remote Sens. Environ.* **2017**, *201*, 47–56. [CrossRef]
13. Werther, M.; Odermatt, D.; Simis, S.G.H.; Gurlin, D.; Lehmann, M.K.; Kutser, T.; Gupana, R.; Varley, A.; Hunter, P.D.; Tyler, A.N.; et al. A Bayesian Approach for Remote Sensing of Chlorophyll-*a* and Associated Retrieval Uncertainty in Oligotrophic and Mesotrophic Lakes. *Remote Sens. Environ.* **2022**, *283*, 113295. [CrossRef]
14. Wang, S.; Jiang, X.; Spyrakos, E.; Li, J.; Mcglinchey, C.; Constantinescu, A.M.; Tyler, A.N. Water Color from Sentinel-2 MSI Data for Monitoring Large Rivers: Yangtze and Danube. *Geo-Spat. Inf. Sci.* **2023**, *27*, 854–869. [CrossRef]
15. Gordon, H.R.; Wang, M. Surface-Roughness Considerations for Atmospheric Correction of Ocean Color Sensors. II: Error in the Retrieved Water-Leaving Radiance. *Appl. Opt.* **1992**, *31*, 4261–4267. [CrossRef] [PubMed]
16. Warren, M.A.; Simis, S.G.H.; Martinez-Vicente, V.; Poser, K.; Bresciani, M.; Alikas, K.; Spyrakos, E.; Giardino, C.; Ansper, A. Assessment of Atmospheric Correction Algorithms for the Sentinel-2A MultiSpectral Imager over Coastal and Inland Waters. *Remote Sens. Environ.* **2019**, *225*, 267–289. [CrossRef]
17. Sullivan, S.A. Experimental Study of the Absorption in Distilled Water, Artificial Sea Water, and Heavy Water in the Visible Region of the Spectrum*. *J. Opt. Soc. Am.* **1963**, *53*, 962–968. [CrossRef]

18. Chen, S.; Hu, C. Estimating Sea Surface Salinity in the Northern Gulf of Mexico from Satellite Ocean Color Measurements. *Remote Sens. Environ.* **2017**, *201*, 115–132. [CrossRef]
19. Cao, Z.; Ma, R.; Duan, H.; Pahlevan, N.; Melack, J.; Shen, M.; Xue, K. A Machine Learning Approach to Estimate Chlorophyll-*a* from Landsat-8 Measurements in Inland Lakes. *Remote Sens. Environ.* **2020**, *248*, 111974. [CrossRef]
20. Cao, Z.; Wang, M.; Ma, R.; Zhang, Y.; Duan, H.; Jiang, L.; Xue, K.; Xiong, J.; Hu, M. A Decade-Long Chlorophyll-a Data Record in Lakes across China from VIIRS Observations. *Remote Sens. Environ.* **2024**, *301*, 113953. [CrossRef]
21. Pyo, J.; Duan, H.; Baek, S.; Kim, M.S.; Jeon, T.; Kwon, Y.S.; Lee, H.; Cho, K.H. A Convolutional Neural Network Regression for Quantifying Cyanobacteria Using Hyperspectral Imagery. *Remote Sens. Environ.* **2019**, *233*, 111350. [CrossRef]
22. Shen, M.; Duan, H.; Cao, Z.; Xue, K.; Qi, T.; Ma, J.; Liu, D.; Song, K.; Huang, C.; Song, X. Sentinel-3 OLCI Observations of Water Clarity in Large Lakes in Eastern China: Implications for SDG 6.3.2 Evaluation. *Remote Sens. Environ.* **2020**, *247*, 111950. [CrossRef]
23. Urquhart, E.A.; Zaitchik, B.F.; Hoffman, M.J.; Guikema, S.D.; Geiger, E.F. Remotely Sensed Estimates of Surface Salinity in the Chesapeake Bay: A Statistical Approach. *Remote Sens. Environ.* **2012**, *123*, 522–531. [CrossRef]
24. Bayati, M.; Danesh-Yazdi, M. Mapping the Spatiotemporal Variability of Salinity in the Hypersaline Lake Urmia Using Sentinel-2 and Landsat-8 Imagery. *J. Hydrol.* **2021**, *595*, 126032. [CrossRef]
25. Dai, J.; Liu, T.; Zhao, Y.; Tian, S.; Ye, C.; Nie, Z. Remote Sensing Inversion of the Zabuye Salt Lake in Tibet, China Using LightGBM Algorithm. *Front. Earth Sci.* **2023**, *10*, 1022280. [CrossRef]
26. Ma, R.; Yang, G.; Duan, H.; Jiang, J.; Wang, S.; Feng, X.; Li, A.; Kong, F.; Xue, B.; Wu, J.; et al. China's Lakes at Present: Number, Area and Spatial Distribution. *Sci. China-Earth Sci.* **2011**, *54*, 283–289. [CrossRef]
27. Yang, F.; Wen, B.; Li, X.; Yang, Y.; Wang, S.; Ou, Y.; Liu, W.; Wang, Z.; Meng, X.; Li, C.; et al. Investigation of Water Environment and Fish Diversity in Dalinor Wetlands I. Major Ions, Salt Content and Electrical Conductivity in the Water of Dali Lake. *Wetl. Sci.* **2020**, *18*, 507–515.
28. Li, X.; Liu, Y.; Zhang, S.; Shi, X.; Li, W.; Sun, B.; Zhao, S. Spatiotemporal Variation of Phytoplankton Community Structure and Its Influencing Factors in the Dalinor Lake. *Wetl. Sci.* **2023**, *21*, 897–906.
29. Xu, C. Bacterial Diversity in the Water and Sediment of Daihai Lake. Master's Thesis, Shanghai Ocean University, Shanghai, China, 2023.
30. Kloiber, S.M.; Brezonik, P.L.; Olmanson, L.G.; Bauer, M.E. A Procedure for Regional Lake Water Clarity Assessment Using Landsat Multispectral Data. *Remote Sens. Environ.* **2002**, *82*, 38–47. [CrossRef]
31. Mobley, C.D. Estimation of the Remote-Sensing Reflectance from above-Surface Measurements. *Appl. Opt.* **1999**, *38*, 7442–7455. [CrossRef]
32. Mueller, J.L.; Morel, A.; Frouin, R.; Davis, C.; Arnone, R.; Carder, K.; Lee, Z.P.; Steward, R.G.; Hooker, S.; Mobley, C.D. *Ocean Optics Protocols For Satellite Ocean Color Sensor Validation, Revision 4. Volume III: Radiometric Measurements and Data Analysis Protocols*; Goddard Space Flight Center: Greenbelt, MD, USA, 2003.
33. Lorenzen, C. Determination of Chlorophyll and Pheo-Pigments—Spectrophotometric Equations. *Limnol. Oceanogr.* **1967**, *12*, 343–346. [CrossRef]
34. Zhang, Y.; Zhang, B.; Ma, R.; Feng, S.; Le, C. Optically Active Substances and Their Contributions to the Underwater Light Climate in Lake Taihu, a Large Shallow Lake in China. *Fundam. Appl. Limnol.* **2007**, *170*, 11–19. [CrossRef]
35. Muñoz Sabater, J. ERA5-Land Monthly Averaged Data from 1950 to Present. 2019. Available online: https://cds.climate.copernicus.eu/datasets/reanalysis-era5-land-monthly-means?tab=overview (accessed on 10 August 2024).
36. Lehner, B.; Grill, G. Global River Hydrography and Network Routing: Baseline Data and New Approaches to Study the World's Large River Systems. *Hydrol. Process.* **2013**, *27*, 2171–2186. [CrossRef]
37. Otsu, N. Threshold Selection Method from Gray-Level Histograms. *IEEE Trans. Syst. Man Cybern.* **1979**, *9*, 62–66. [CrossRef]
38. Knaeps, E.; Ruddick, K.G.; Doxaran, D.; Dogliotti, A.I.; Nechad, B.; Raymaekers, D.; Sterckx, S. A SWIR Based Algorithm to Retrieve Total Suspended Matter in Extremely Turbid Waters. *Remote Sens. Environ.* **2015**, *168*, 66–79. [CrossRef]
39. Vanhellemont, Q. Adaptation of the Dark Spectrum Fitting Atmospheric Correction for Aquatic Applications of the Landsat and Sentinel-2 Archives. *Remote Sens. Environ.* **2019**, *225*, 175–192. [CrossRef]
40. Doerffer, R.; Schiller, H. The MERIS Case 2 Water Algorithm. *Int. J. Remote Sens.* **2007**, *28*, 517–535. [CrossRef]
41. Brockmann, C.; Doerffer, R.; Peters, M.; Kerstin, S.; Embacher, S.; Ruescas, A. Evolution of the C2RCC Neural Network for Sentinel 2 and 3 for the Retrieval of Ocean Colour Products in Normal and Extreme Optically Complex Waters. In Proceedings of the Living Planet Symposium, Prague, Czech Republic, 9–13 May 2016; Volume 740, p. 54.
42. Antoine, D.; Morel, A. Relative Importance of Multiple Scattering by Air Molecules and Aerosols in Forming the Atmospheric Path Radiance in the Visible and Near-Infrared Parts of the Spectrum. *Appl. Opt.* **1998**, *37*, 2245–2259. [CrossRef]
43. Steinmetz, F.; Deschamps, P.-Y.; Ramon, D. Atmospheric Correction in Presence of Sun Glint: Application to MERIS. *Opt. Express* **2011**, *19*, 9783–9800. [CrossRef]
44. Ruddick, K.G.; Ovidio, F.; Rijkeboer, M. Atmospheric Correction of SeaWiFS Imagery for Turbid Coastal and Inland Waters. *Appl. Optics* **2000**, *39*, 897–912. [CrossRef]
45. De Keukelaere, L.; Sterckx, S.; Adriaensen, S.; Knaeps, E.; Reusen, I.; Giardino, C.; Bresciani, M.; Hunter, P.; Neil, C.; Van der Zande, D.; et al. Atmospheric Correction of Landsat-8/OLI and Sentinel-2/MSI Data Using iCOR Algorithm: Validation for Coastal and Inland Waters. *Eur. J. Remote Sens.* **2018**, *51*, 525–542. [CrossRef]

46. Main-Knorn, M.; Pflug, B.; Louis, J.; Debaecker, V.; Muller-Wilm, U.; Gascon, F. Sen2Cor for Sentinel-2. In Proceedings of the Image and Signal Processing for Remote Sensing XXIII, Warsaw, Poland, 11–14 September 2017; Bruzzone, L., Bovolo, F., Eds.; Spie-Int Soc Optical Engineering: Bellingham, WA, USA, 2017; Volume 10427, p. 1042704.
47. Chen, T.; Guestrin, C. XGBoost: A scalable tree boosting system. In Proceedings of the 22nd ACM SIGKDD International Conference on Knowledge Discovery and Data Mining, San Francisco, CA, USA, 13–17 August 2016; Assoc Computing Machinery: New York, NY, USA, 2016; pp. 785–794.
48. Lyons, M.B.; Keith, D.A.; Phinn, S.R.; Mason, T.J.; Elith, J. A Comparison of Resampling Methods for Remote Sensing Classification and Accuracy Assessment. *Remote Sens. Environ.* **2018**, *208*, 145–153. [CrossRef]
49. Sen, P.K. Estimates of the Regression Coefficient Based on Kendall's Tau. *J. Am. Stat. Assoc.* **1968**, *63*, 1379–1389. [CrossRef]
50. Hu, C. Remote Detection of Marine Debris Using Sentinel-2 Imagery: A Cautious Note on Spectral Interpretations. *Mar. Pollut. Bull.* **2022**, *183*, 114082. [CrossRef] [PubMed]
51. Vanhellemont, Q.; Ruddick, K. Atmospheric Correction of Metre-Scale Optical Satellite Data for Inland and Coastal Water Applications. *Remote Sens. Environ.* **2018**, *216*, 586–597. [CrossRef]
52. Harmel, T.; Chami, M.; Tormos, T.; Reynaud, N.; Danis, P.-A. Sunglint Correction of the Multi-Spectral Instrument (MSI)-SENTINEL-2 Imagery over Inland and Sea Waters from SWIR Bands. *Remote Sens. Environ.* **2018**, *204*, 308–321. [CrossRef]
53. Feng, L.; Hu, C.; Chen, X.; Tian, L.; Chen, L. Human Induced Turbidity Changes in Poyang Lake between 2000 and 2010: Observations from MODIS. *J. Geophys. Res.-Oceans* **2012**, *117*, C07006. [CrossRef]
54. Siddorn, J.R.; Bowers, D.G.; Hoguane, A.M. Detecting the Zambezi River Plume Using Observed Optical Properties. *Mar. Pollut. Bull.* **2001**, *42*, 942–950. [CrossRef]
55. Liu, C.; Zhu, L.; Wang, J.; Ju, J.; Ma, Q.; Kou, Q. The Decrease of Salinity in Lakes on the Tibetan Plateau between 2000 and 2019 Based on Remote Sensing Model Inversions. *Int. J. Digit. Earth* **2023**, *16*, 2644–2659. [CrossRef]
56. Smith, R.C.; Baker, K.S. Optical Properties of the Clearest Natural Waters (200–800 nm). *Appl. Opt.* **1981**, *20*, 177–184. [CrossRef]
57. Mobley, C.D. The Optical Properties of Water. In *Handbook of Optics*; McGraw-Hill: New York, NY, USA, 1995; Volume 1, ISBN 0-07-047740-X.
58. Rusuli, Y.; Li, L.; Ahmad, S.; Zhao, X. Dynamics Model to Simulate Water and Salt Balance of Bosten Lake in Xinjiang, China. *Environ. Earth Sci.* **2015**, *74*, 2499–2510. [CrossRef]
59. Jiang, X.; Fan, C.; Liu, K.; Chen, T.; Cao, Z.; Song, C. Centenary Covariations of Water Salinity and Storage of the Largest Lake of Northwest China Reconstructed by Machine Learning. *J. Hydrol.* **2022**, *612*, 128095. [CrossRef]
60. Guo, M.; Zhou, X.; Li, J.; Wu, W.; Chen, Y. Assessment of the Salinization Processes in the Largest Inland Freshwater Lake of China. *Stoch. Environ. Res. Risk Assess.* **2015**, *29*, 1823–1833. [CrossRef]
61. Liu, X.; Zhang, G.; Zhang, J.; Xu, Y.J.; Wu, Y.; Wu, Y.; Sun, G.; Chen, Y.; Ma, H. Effects of Irrigation Discharge on Salinity of a Large Freshwater Lake: A Case Study in Chagan Lake, Northeast China. *Water* **2020**, *12*, 2112. [CrossRef]
62. Lu, Y.; Li, Y.; Lin, P.; Cheng, L.; Ge, K.; Liu, H.; Duan, J.; Wang, F. North Atlantic-Pacific Salinity Contrast Enhanced by Wind and Ocean Warming. *Nat. Clim. Chang.* **2024**, *14*, 723–731. [CrossRef]
63. Yihdego, Y.; Webb, J. Modelling of Seasonal and Long-Term Trends in Lake Salinity in Southwestern Victoria, Australia. *J. Environ. Manag.* **2012**, *112*, 149–159. [CrossRef]
64. Sun, M.; Zhang, L.; Yang, R.; Li, X.; Zhao, J.; Liu, Q. Water Resource Dynamics and Protection Strategies for Inland Lakes: A Case Study of Hongjiannao Lake. *J. Environ. Manag.* **2024**, *355*, 120462. [CrossRef]
65. Ma, X.; Huang, S.; Huang, Y.; Wang, X.; Luo, Y. Evaporation from the Hypersaline Aral Sea in Central Asia. *Sci. Total Environ.* **2024**, *908*, 168412. [CrossRef]
66. Wurtsbaugh, W.A.; Miller, C.; Null, S.E.; DeRose, R.J.; Wilcock, P.; Hahnenberger, M.; Howe, F.; Moore, J. Decline of the World's Saline Lakes. *Nat. Geosci.* **2017**, *10*, 816–821. [CrossRef]
67. Zhou, Y.; Jiang, J. Changes in the Ecological Environment in the Daihai Lake Basin over the Last 50 Years. *Arid Zone Res.* **2009**, *26*, 162–168. [CrossRef]
68. Aladin, N.V.; Gontar, V.I.; Zhakova, L.V.; Plotnikov, I.S.; Smurov, A.O.; Rzymski, P.; Klimaszyk, P. The Zoocenosis of the Aral Sea: Six Decades of Fast-Paced Change. *Environ. Sci. Pollut. Res.* **2019**, *26*, 2228–2237. [CrossRef]
69. Moore, J.N. Recent Desiccation of Western Great Basin Saline Lakes: Lessons from Lake Abert, Oregon, USA. *Sci. Total Environ.* **2016**, *554*, 142–154. [CrossRef] [PubMed]
70. Liu, H.; Xiao, S.; Liu, W.; Wang, H.; Liu, Z.; Li, X.; Zhang, P.; Liu, J. Salinity Decreases Methane Concentrations in Chinese Lakes. *Sci. Total Environ.* **2024**, *937*, 173412. [CrossRef] [PubMed]
71. UN-Water. *Integrated Monitoring Guide for SDG 6: Targets and Global Indicators*; UN-Water: New York, NY, USA, 2016.
72. United Nations. *The Sustainable Development Goals Report 2024*; United Nations: Geneva, Switzerland, 2024.